

Tunable narrow-band single-channel add-drop integrated optical filter with ultrawide FSR

Chunlei Sun

Westlake University

Yuexin Yin

Jilin University

Zequn Chen

Westlake University

Yuting Ye

Westlake University

Ye Luo

Westlake University

Hui Ma

Zhejiang University

Lichun Wang

Zhejiang University

Maoliang Wei

Zhejiang University

Jialing Jian

Westlake University

Renjie Tang

Westlake University

Hao Dai

Zhejiang University

Jianghong Wu

Westlake University

Junying Li

Zhejiang University

Daming Zhang

Jilin University

Hongtao Lin

Zhejiang University

Lan Li (✉ lilan@westlake.edu.cn)

Westlake University <https://orcid.org/0000-0002-9097-9157>

Research Article

Keywords: Integrated devices, Silicon photonics, Optical filters, FSR-free filters, Tunable filters

Posted Date: April 5th, 2022

DOI: <https://doi.org/10.21203/rs.3.rs-1193735/v1>

License:   This work is licensed under a Creative Commons Attribution 4.0 International License.

[Read Full License](#)

Abstract

Free-spectral-range (FSR)-free optical filters have always been a critical challenge for photonic integrated circuits. A high-performance FSR-free filter is highly desired for communication, spectroscopy, and sensing applications. Despite significant progress in integrated optical filters, the FSR-free filter with a tunable narrow-band, high out-of-band rejection, and large fabrication tolerance has rarely been demonstrated. In this paper, we propose an exact and robust design method for add-drop filters (ADFs) with an FSR-free operation capability, a sub-nanometer optical bandwidth, and a high out-of-band rejection (OBR) ratio. The achieved filter has a 3-dB bandwidth of < 0.5 nm and an OBR ratio of 21.5 dB within a large waveband of 220 nm, which to the best of our knowledge, is the largest-FSR ADF demonstrated on a silicon photonic platform. The filter exhibits large tunability of 12.3 nm with a heating efficiency of 97 pm/mW and maintains the FSR-free feature in the whole tuning process. In addition, we fabricated a series of ADFs with different periods, which all showed reliable and excellent performances.

Introduction

Free-spectral-range (FSR)-free optical filters with the ability to selectively manipulate wavelengths within a large waveband have many advanced applications such as optical communication[1–4], parallel optical computing[5–8], spectroscopic sensing[9–12], as well as single-wavelength laser[13–15]. An FSR-free filter can significantly increase the number of information channels for large-capacity optical communication and realize the multi-loci and multiparameter sensing through cascaded independent functional units on a single sensor link. A straightforward method to obtain an FSR-free response across the entire wavelength range is utilizing the photonic bandgap feature of Bragg grating. Bragg gratings waveguide/fibers from the inscription of a Bragg grating in a waveguide/fiber have been extensively investigated in academia and industry. Bragg-grating-assisted contra-directional couplers (contra-DC) can serve as an add-drop filter (ADF) to avoid a circulator for separating the reflected light back from the Bragg gratings waveguide [16, 17]. Nevertheless, directly utilizing the stopband of the Bragg grating practically limits the applications due to the box-like broadband response. Although weakening the grating strength can reduce the bandwidth, the grating could be quite long[18, 19]. Another way to significantly enlarge the filter's FSR is to apply the Vernier effect in multiple cascaded microring resonators with slightly different radii[3, 20–22]. The microring-based filters usually suffer from severe side modes. The wavelength alignment needs a complex calibrating and tuning process. Therefore, it is difficult to scan the resonance wavelength continuously and quickly. Up to now, various mixed complex strategies have been applied to realize an FSR-free response by either optimizing the device design or carefully calibrating and tuning the optical filter.

We recently experimentally demonstrated a filter that features an FSR-free operation capability and a sub-nanometer optical bandwidth by utilizing a side-coupled Bragg-grating-assisted Fabry–Perot (F-P) cavity without any need for calibration and tuning[23]. In contrast to Bragg gratings waveguide and contra-DC giving a box-like optical response, our previously proposed architecture introduces a point-defect in the Bragg grating to form the Fabry–Perot filter exhibiting an ultrasharp dip optical response over a broad

wavelength range. However, only two ports are available, potentially limiting its communication and sensing applications. On the other hand, reconfigurable photonic integrated devices are being developed to efficiently optimize and flexibly utilize bandwidth/channel resources, playing a significant role in intelligent photonic networks. Combining extra tunability with the FSR-free feature can realize reconfigurable optical ADFs in future intelligent optical networks supporting hitless wavelength switching[3]. In addition, the wavelength tunability can effectively reduce the number of filters and facilitate their further development in high-resolution on-chip spectroscopy[12].

In this article, we propose an ADF by utilizing three coupled waveguides with a central grating-assisted F-P cavity implemented on a silicon-on-insulator (SOI) platform and experimentally demonstrate only one single resonance within ultrabroad waveband. Importantly, we provide a strict FSR-free condition to design ADFs through comprehensive analysis and optimization. Note that there have been recently reported ADFs based on three coupled waveguides with nanobeam cavities[24–29]. However, the nanobeam cavity has a stopband of typically hundreds of nanometers, supporting multiple in-band resonance modes. The essential advantage of our proposed device is to support the FSR-free operation and hitless wavelength tuning. The fabricated filter indicates an out-of-band rejection (OBR) ratio of 21.5 dB and narrow bandwidth of 0.5 nm at the drop port, and the filter can be tuned with a wavelength shift of 12.3 nm and still maintains the FSR-free feature.

Results And Discussion

Device design and operation principle

Figure 1a shows the proposed filter architecture consisting of a central grating-assisted F-P cavity and two symmetrically side-coupled bend waveguides. The F-P cavity consists of a central waveguide with length L_c , two identical tapered gratings, and two Bragg gratings. The Bragg gratings are designed as two symmetrical mirrors to reflect the light to the central waveguide. Each grating is formed by side etching single-mode waveguide to get narrow transoms with width d periodically, as shown in Fig. 1b. The period is Λ , and the duty circle is 0.5. The tapered gratings connect the central waveguide and Bragg grating to reduce the scattering loss and satisfy the phase-matching condition between the fundamental Bloch and the waveguide modes. The curved waveguides are used to couple the light into and out of the central waveguide with the waveguide-input-cavity coupling gap g_1 and the cavity-output-waveguide coupling gap g_2 , as shown in the cross-section view (Fig. 1c). The resonance tuning is actuated by a thermo-optical heater deposited over the F-P cavity. In addition, a scanning electron micrograph (SEM) was conducted to check the etching quality of the three coupled waveguides with the F-P cavity, as shown in Fig. 1d.

The proposed ADF is similar to a traditional one except for two symmetric Bragg gratings as the mirrors and band-stop filters. Instead of supporting the traveling wave in a conventional ADF's cavity, such as a ring/disk resonator, the cavity of the proposed ADF supports a pure standing wave. The operating

principle can be formulated by the coupled-mode theory[30]. The power P_R reflected from the input port, the transmission power P_{T1} through port T1, and both drop ports D1,2 can be expressed as follows:

$$P_R = \frac{\frac{1}{\tau^2}}{(\omega - \omega_0)^2 + (\frac{1}{\tau} + \frac{1}{\tau_o} + \frac{1}{\tau})^2} \#(1.)$$

$$P_{T1} = \frac{(\omega - \omega_0)^2 + (\frac{1}{\tau_o} + \frac{1}{\tau})^2}{(\omega - \omega_0)^2 + (\frac{1}{\tau} + \frac{1}{\tau_o} + \frac{1}{\tau})^2} \#(2.)$$

$$P_{D1,2} = \frac{\frac{1}{\tau\tau}}{(\omega - \omega_0)^2 + (\frac{1}{\tau} + \frac{1}{\tau_o} + \frac{1}{\tau})^2} \#(3.)$$

where ω_0 is the resonant frequency, $\frac{1}{\tau_o}$ is the decay rate due to loss, $\frac{1}{\tau}$ and $\frac{1}{\tau}$ are the rates of decay into the input and output curved waveguides. At the resonance of $\omega = \omega_0$ and the condition of $\frac{1}{\tau} = \frac{1}{\tau_o} + \frac{1}{\tau}$, the resonant mode decays equally into the forward and the backward propagating waveguide mode. The power transferred into the output waveguide at resonance is maximized; we can find $P_R = P_{T1} = 0.25$, $P_{D1,2} = 0.25(1 - \frac{\tau}{\tau_o})$. For the case of strong coupling between the input waveguide and the cavity with an ultralarge $\frac{1}{\tau}$, the power is equally distributed into drop ports D1 and D2, near 0.25. The method to increase the drop efficiency will be discussed in detail later.

The calculated transmission spectra of the designed filter at drop ports (D1 and D2) and through port (T1) are attained by the three-dimensional finite-difference time-domain (3D FDTD) method, as shown in Fig. 2a. These simulation parameters are $R_r=20 \mu\text{m}$, $w=500 \text{ nm}$, $d=300 \text{ nm}$, $\Lambda=316 \text{ nm}$, $L_c=0 \mu\text{m}$, $g_1=200 \text{ nm}$, $g_2=250 \text{ nm}$, $N_1=5$ and $N_2=150$, respectively. It can be observed that only one single resonant mode is excited at D1 and D2 ports from 1400 to 1630 nm. Across the entire wavelength range, the in-band insertion loss at drop ports is about -6.5 dB (drop efficiency ~ 0.22), which agrees well with the theoretical analysis. The OBR at the drop port is about 16 dB. Figure 2b exhibits the electric field distribution of the whole structure at the wavelengths of 1400, 1516, and 1630 nm. At the resonant wavelength of 1516 nm, the light is almost equally divided into four parts. At non-resonant wavelengths, the filter is considered a tri-waveguide directional coupler. The light propagates to the T1 port directly, while very little light is transmitted to the D2 port. Thus, the optical power at the D2 port is larger than that at the D1 port.

The spectral response of our proposed filter depends mainly on the FSR_{FP} of the F-P cavity with an ideal reflector and the stopband of the Bragg grating $\Delta\lambda_{\text{sb}}$. The strict FSR-free condition is $\Delta\lambda_{\text{sb}} < \text{FSR}_{\text{FP}}$, only one resonant mode of the F-P cavity in the stopband of Bragg grating is excited. The FSR-free condition can also be satisfied by $\text{FSR}_{\text{FP}} < \Delta\lambda_{\text{sb}} < 2\text{FSR}_{\text{FP}}$ only when the resonant wavelength is around the central

wavelength of the stopband λ_c ; otherwise, there exist two resonant modes. Considering that 3D FDTD simulation for the entire device is time-consuming, it is challenging to study the relationship between the device response and the key parameters profoundly and determine the device geometry with the FSR-free operation capability at the desired wavelength range by 3D FDTD.

In this case, the investigation of the coupled-mode theory seems particularly important. For the Bragg grating, it is known that the optical rejection R_e and $\Delta\lambda_{sb}$ of the Bragg grating are decided by the grating geometry[31]

$$R_e = \tanh^2(\kappa L_g) \#(4.)$$

$$\Delta\lambda_{sb} = \frac{\lambda_0^2}{\pi n_g} \sqrt{\kappa^2 + \frac{\pi^2}{L_g^2}} \#(5.)$$

where λ_0 , n_g , κ , and L_g are the central wavelength of stopband, the group index, the coupling coefficient, and the grating length. λ_0 is decided by the Bragg phase-matching condition $\lambda_0 = 2\Lambda n_{eff}$, n_{eff} is the effective index of the mode propagating through the grating. Once the geometry of the grating is given, $\Delta\lambda_{sb}$, κ , and n_g can be acquired by the 3D eigenmode expansion (3D EME) simulation algorithm according to Equations (4) and (5). The 3D EME algorithm is an exact and efficient simulation tool. Specially, it is much more time-saving than 3D FDTD for periodic structures. The FSR is given by

$$FSR_{FP} = \frac{\lambda_0^2}{2(L_c n_{g1} + 2L_{pd} n_g + 2L_t n_{g2})} \#(6.)$$

where L_{pd} and L_t are the penetration depth of the Bragg grating and the length of the tapered grating. n_{g1} , n_g , and n_{g2} are the group refractive indices of central waveguide, Bragg grating, and the tapered grating, respectively. L_{pd} can be given by effective refraction index of wide and narrow parts of the Bragg grating n_n and n_w [32]

$$L_{pd} = \frac{1}{2} \left(\frac{\lambda_0}{4n_n} + \frac{\lambda_0}{4n_w} \right) / \ln \left(\frac{n_w}{n_n} \right) \#(7.)$$

The contour plots of the calculated $\Delta\lambda_{sb}$, FSR_{FP} , and ratio $R = \Delta\lambda_{sb} / FSR_{FP}$ are shown in Figs. 3a-3c, respectively, as functions of Λ and d . Note that the dispersion of effective refraction index and group index has been considered for the whole calculation process. The waveguide width w and L_c are 0.5 μm and 0 μm , respectively. As shown in Fig. 3c, Λ is almost independent of the ratio R , which is more sensitive to the variation of d . Figure 3d exhibits a contour map of the calculated R as a function of L_c and d for $\Lambda = 316$ nm. The ratio R has a strong correlation with L_c and d . The white and blue contour lines

of $R = 1$ and $R = 2$ in Figs. 3c and 3d divide the figures into three areas, corresponding to the three cases discussed in our previous work[23]. Therefore, the contour maps provide useful guidance for designing an FSR-free filter.

We further simulated temperature field distributions at different bias voltages using the finite-element solver to confirm the filter's external wavelength tuning performance. The waveguide was embedded between the 3- μm -thick buried oxide as the bottom layer and the 1- μm -thick oxide as the top cladding layer. 100-nm-thick titanium (Ti) and 100-nm-thick gold (Au) serve as microheaters and contact pads. The device was simulated with the bias voltage set from 2 to 5 V. We can observe the obvious temperature rise in the waveguide, as shown in Fig. 4a. Figure 4b shows the transmission spectra with the bias voltage set from 0 to 6 V by 3D FDTD simulations. The resonant wavelength redshifts with the increasing bias voltage and the FSR-free operation feature has been observed for all the tuning configurations.

For device characterization, a broadband tunable laser system (Santec full-band TSL, 1260–1630 nm) is employed to characterize the fabricated devices. We also fabricated and characterized a reference structure near the proposed filter on the same chip. The reference structure comprises two grating couplers and a straight waveguide of 200 microns in length. Our proposed filter is connected by the grating couplers with the same parameters at both ends to facilitate characterization. Considering that the propagation loss of the straight waveguide can be ignored, the response spectra of the filter can be obtained by subtracting the insertion loss of the reference structure. The grating coupler with a 150-nm etching depth has a peak coupling efficiency of -7.5 dB and a 10-dB bandwidth of ~ 200 nm, which is much broader than that of the shallow-etched grating couplers with a 70-nm etching depth.

Figure 5 shows the normalized spectral response at D1 and T1 ports for the fabricated optical filter associated with various pitches. The critical parameters of $R_f = 20 \mu\text{m}$, $w = 500 \text{ nm}$, $d = 300 \text{ nm}$, $L_c = 0 \mu\text{m}$, $g_1 = 350 \text{ nm}$, $g_2 = 300 \text{ nm}$, $N_1 = 5$, and $N_2 = 150$ are adopted. As the pitch Λ deviates from 292 to 316 nm with a 6 nm interval, the resonant wavelength has a redshift from 1431.3 to 1505.9 nm. We can only observe a single sharp peak with an OBR of ~ 21.5 dB in a 220-nm wavelength span from 1360 to 1580 nm at the D1 port. The strong noises from 1360 to 1420 nm result from the limited bandwidth of the grating coupler. The insertion loss is lower than 8.4 dB, and the 3-dB bandwidth is smaller than 0.5 nm. Figure 6a shows the measured spectral responses at the D1 and T1 ports of the fabricated optical filter with $\Lambda = 298 \text{ nm}$, which demonstrates the tunability and provides a guide to accurate wavelength routing. When the applied bias voltage for heating varied from 0 to 8 V in the experiments, the wavelength can be tuned with a wavelength shift of $\sim 12.3 \text{ nm}$. The inset shows the zoom-in view of the resonant peaks. There is a linear relationship between the resonant wavelength shift and the heating power, as shown in Fig. 6b. The thermo-tuning efficiency, namely, the slope of the fitted curve, is 97 pm/mW, which can be further increased by improving the alignment between the waveguide and the microheater. In addition, the tuning range can be increased to about 30 nm by utilizing isolation trenches surrounding the filter[33]. Compared to the microheater without trenches, the one with trenches can avoid heat dissipation from the side to enhance the heating efficiency. However, the maximum resonance wavelength shift will be limited by the highest power the microheater could withstand. As a result, it is difficult to cover the entire FSR-free

range via heating due to the small thermo-optic coefficient of silicon (1.86×10^{-4} at 1550 nm). However, tens of nanometers of tuning range are also meaningful and enable a lot of applications in sensing, communication, and spectroscopy. The 3-dB bandwidth and the insertion loss variation are smaller than 0.17 nm and 1.1 dB, respectively, as shown in Fig. 6c.

Discussion

As previously discussed, one of the critical parameters of our proposed filter, drop efficiency, is quite limited to a small number. Breaking bidirectional coupling to suppress contra-coupling can effectively increase the drop efficiency [24, 25, 28, 29]. Recently, a semi-symmetric Fano structure has been proposed by inserting a partially transmitting element into the bend waveguide side-coupled with a cavity [24]. Thus, Fano resonance is realized in a nanophotonic filter to obtain high drop port transmission. The four holes added on two side-coupled waveguides must be designed and fabricated elaborately. Multimode Bragg grating reflectors separated by a multimode waveguide instead of the single-mode ones are also utilized for mode conversion between the fundamental and higher-order modes due to phase-matching conditions [25, 34]. The fields in the cavity and bend waveguide are coupled only in the forward direction. Nevertheless, the rigorous phase matching is sensitive to fabrication error. The performance of both methods may degrade under extensive external tuning. In addition, a dual photonic crystal nanobeam cavity system serves as a traveling wave resonator, separating the transmission of the through and drop port from the input port. These two cavities must be fabricated perfectly to align the resonant wavelengths. To look for a robust method to increase the drop efficiency, we investigate the phase of both drop ports of the proposed ADF. Figure 7a shows the phase difference of the drop ports. At the resonance wavelength as the yellow star shows in Fig. 7a, the phase difference is π . It is well known that a 2×2 adiabatic splitter can be utilized as a 3-dB coupler. The phase difference between the output ports of 2×2 adiabatic splitter is 0 or π , which depends on the input port of incident light [35, 36]. Therefore, we can combine the transmission from both drop ports using a 2×2 adiabatic splitter to connect the proposed ADF and subsequently double the drop efficiency. The simulated transmission of the improved device combining the 2×2 adiabatic splitter and the proposed ADF is demonstrated in Fig. 7b. The peak drop efficiency is enhanced to be -3.6 dB. We believe that the scheme has high reliability since the 2×2 adiabatic splitter is typically robust, has broad bandwidth and large fabrication tolerance.

Conclusions

In summary, we have theoretically and experimentally demonstrated an FSR-free filter at the entire waveband with hitless tuning. A rapid and exact design method of the FSR-free filter with a narrow band and high OBR has been developed. The demonstrated filters show only one peak in a 220 nm wavelength span from 1360 to 1580 nm. The measured OBR is as high as 21.5 dB, and the 3-dB bandwidth is as narrow as 0.5 nm. The filter exhibits large tunability of 12.3 nm with a heating efficiency of 97 pm/mW and allows the FSR-free feature to be maintained for all the tuning configurations. We expect that these

results may contribute to opening the door to new applications in large-capacity optical communication, optical computing, spectroscopic sensing, and advanced tunable lasing.

Methods

Micro/Nano Fabrication of the filter

The proposed filter was patterned on an SOI platform with a top silicon thickness of 220 nm by electron beam lithography (EBL, Raith Voyager) and subsequent inductively coupled plasma (ICP, Samco). To leverage the convenience of single-step EBL and ICP etching, the focusing grating couplers employed for off-chip coupling and the FSR-free filter both have an etching depth of 150 nm. Then a 1- μm -thick layer of silicon oxide was deposited on the chip surface by plasma-enhanced chemical vapor deposition (PECVD) to cover the device. Finally, The metal titanium and gold with different thickness combinations were deposited by an E-beam evaporator to realize microheaters (100 nm Ti/ 10 nm Au) and contact pads (10 nm Ti/ 100 nm Au). The width of the Ti heater is 2.75 μm .

Abbreviations

FSR

Free spectral range

ADFs

Add-drop filters

OBR

Out-of-band rejection

SOI

Silicon-on-insulator

SEM

Scanning electron micrograph

EME

Eigenmode expansion

EBL

Electron beam lithography

ICP

Inductively coupled plasma

PECVD

Plasma-enhanced chemical vapor deposition

Declarations

Acknowledgment.

We thank Westlake Center for Micro/Nano Fabrication and Instrumentation, Service Center for Physical Sciences and Molecular Sciences at Westlake University, and ZJU Micro-Nano Fabrication Center at Zhejiang University for the facility support.

Authors' contributions

CLS and YXY conceived the original idea and designed the experiment. ZQC, YTY, YL, YYL, HM, LHW, HD, MLW, JLJ, RJT, JHW fabricated the devices. CLS, YXY, and ZQC conducted optical characterizations. All authors analyzed the experimental results and contributed to writing and proofreading the manuscript. DMZ, HTL, and LL supervised the overall project. All authors reviewed and approved the final manuscript.

Funding

National Key Research and Development Program of China (2019YFB2203003); National Natural Science Foundation of China (62175202 and 91950204); Leading Innovative and Entrepreneur Team Introduction Program of Zhejiang (2020R01005); the Open Research program of Key Laboratory of 3D Micro/Nano Fabrication and Characterization of Zhejiang Province; Westlake University (the start-up fund of Westlake University).

Availability of data and materials

All data generated or analyzed during this study are included in this published article.

Competing interests: The authors declare no competing interests.

References

1. Corcoran B, Tan M, Xu X, Boes A, Wu J, Nguyen TG, et al. Ultra-dense optical data transmission over standard fibre with a single chip source. *Nat Commun.* 2020;11:2568.
2. Dai D, Bowers JE. Silicon-based on-chip multiplexing technologies and devices for Peta-bit optical interconnects. *Nanophotonics.* 2014;3:283–311.
3. Morichetti F, Milanizadeh M, Petrini M, Zanetto F, Ferrari G, De Aguiar DO, et al. Polarization-transparent silicon photonic add-drop multiplexer with wideband hitless tuneability. *Nat Commun.* 2021;12:4324.
4. Baier M, Grote N, Moehrl M, Sigmund A, Soares FM, Theurer M, Troppenz U. Integrated transmitter devices on InP exploiting electro-absorption modulation. *Photonix.* 2020;1:4.
5. Feldmann J, Youngblood N, Karpov M, Gehring H, Li X, Stappers M, et al. Parallel convolutional processing using an integrated photonic tensor core. *Nature.* 2021;589:52–8.
6. Feldmann J, Youngblood N, Wright CD, Bhaskaran H, Pernice WHP. All-optical spiking neurosynaptic networks with self-learning capabilities. *Nature.* 2019;569:208–14.
7. Li C, Zhang X, Li J, Fang T, Dong X. The challenges of modern computing and new opportunities for optics. *Photonix.* 2021;2:20.

8. Goi E, Zhang Q, Chen X, Luan H, Gu M. Perspective on photonic memristive neuromorphic computing. *Photonix*. 2020;1:3.
9. Liu T, Fiore A. Designing open channels in random scattering media for on-chip spectrometers. *Optica*. 2020;7:934–9.
10. Zhang Z, Wang Y, Tsang HK. Tandem Configuration of Microrings and Arrayed Waveguide Gratings for a High-Resolution and Broadband Stationary Optical Spectrometer at 860 nm. *ACS Photon*. 2021;8:1251–7.
11. Xia Z, Eftekhar AA, Soltani M, Momeni B, Li Q, Chamanzar M, et al. High resolution on-chip spectroscopy based on miniaturized microdonut resonators. *Opt Express*. 2011;19:12356–64.
12. Zheng S, Cai H, Song J, Zou J, Liu PY, Lin Z, et al. A Single-Chip Integrated Spectrometer via Tunable Microring Resonator Array. *IEEE Photonics J*. 2019;11:1–9.
13. Wan Y, Zhang S, Norman JC, Kennedy MJ, He W, Liu S, et al. Tunable quantum dot lasers grown directly on silicon. *Optica*. 2019;6:1394–400.
14. Wang R, Sprengel S, Vasiliev A, Boehm G, Van Campenhout J, Lepage G, et al. Widely tunable 2.3 μm III-V-on-silicon Vernier lasers for broadband spectroscopic sensing. *Photonics Res*. 2018;6:858–66.
15. Wan Y, Zhang S, Norman JC, Kennedy MJ, He W, Tong Y, et al. Directly Modulated Single-Mode Tunable Quantum Dot Lasers at 1.3 μm . *Laser Photonics Rev*. 2020;14:1900348.
16. Liu D, Zhang L, Jiang H, Dai D. First demonstration of an on-chip quadplexer for passive optical network systems. *Photonics Res*. 2021;9:757–63.
17. Yun H, Hammood M, Lin S, Chrostowski L, Na FJ. Broadband flat-top SOI add-drop filters using apodized sub-wavelength grating contradirectional couplers. *Opt Lett*. 2019;44:4929–32.
18. Sun H, Chen LR. Polarization-dependent tuning of Bragg reflection enabled through tilted subwavelength grating waveguide Bragg gratings. *Opt Lett*. 2021;46:1450–3.
19. Cheben P, Ctyroky J, Schmid JH, Wang S, Lapointe J, Wanguemert-Perez JG, et al. Bragg filter bandwidth engineering in subwavelength grating metamaterial waveguides. *Opt Lett*. 2019;44:1043–6.
20. Ren Y, Perron D, Aurangozeb F, Jiang Z, Hossain M, Van V. Silicon Photonic Vernier Cascaded Microring Filter for Broadband Tunability. *IEEE Photonics Technol Lett*. 2019;31:1503–6.
21. Boeck R, Jaeger NA, Rouger N, Chrostowski L. Series-coupled silicon racetrack resonators and the Vernier effect: theory and measurement. *Opt Express*. 2010;18:25151–7.
22. Boeck R, Flueckiger J, Yun H, Chrostowski L, Jaeger NA. High performance Vernier racetrack resonators. *Opt Lett*. 2012;37:5199–201.
23. Sun C, Zhong C, Wei M, Ma H, Luo Y, Chen Z, et al. Free-spectral-range-free filters with ultrawide tunability across the S + C + L band. *Photonics Res*. 2021;9:1013–8.
24. Cheng Z, Dong J, Zhang X. Ultracompact optical switch using a single semisymmetric Fano nanobeam cavity. *Opt Lett*. 2020;45:2363–6.

25. Huang Q, Liu Q, Xia J. Traveling wave-like Fabry-Perot resonator-based add-drop filters. *Opt Lett.* 2017;42:5158–61.
26. Soref R, De Leonardis F, Passaro VMN. Compact resonant 2 x 2 crossbar switch using three coupled waveguides with a central nanobeam. *Opt Express.* 2021;29:8751–62.
27. Yu P, Qiu H, Dai T, Cheng R, Lian B, Li W, et al. Ultracompact Channel Add-Drop Filter Based on Single Multimode Nanobeam Photonic Crystal Cavity. *J Lightwave Technol.* 2021;39:162–6.
28. Poulton CV, Zeng X, Wade MT, Popovic MA. Channel add-drop filter based on dual photonic crystal cavities in push-pull mode. *Opt Lett.* 2015;40:4206–9.
29. Alonso-Ramos C, Annoni A, Ortega-Moñux A, Molina-Fernández I, Strain M, Orlandi P, et al. Narrow-band single-channel filter in silicon photonics. San Diego. *Advanced Photonics for Communications Optical Society of America*; 2014.
30. Manolatou C, Khan MJ, Fan S, Villeneuve PR, Haus HA, Joannopoulos JD. Coupling of modes analysis of resonant channel add-drop filters. *IEEE J Quantum Electron.* 1999;35:1322–31.
31. Yariv A. Coupled-mode theory for guided-wave optics. *IEEE J Quantum Electron.* 1973;9:919–33.
32. Koks C, Van Exter MP. Microcavity resonance condition, quality factor, and mode volume are determined by different penetration depths. *Opt Express.* 2021;29:6879–89.
33. Zheng SN, Zou J, Cai H, Song JF, Chin LK, Liu PY, et al. Microring resonator-assisted Fourier transform spectrometer with enhanced resolution and large bandwidth in single chip solution. *Nat Commun.* 2019;10:2349.
34. Ma Y, Zhao Y, Shi Y, Hao L, Sun Z, Hong Z, Chen X. Silicon Add-Drop Multiplexer Based on π Phase-Shifted Antisymmetric Bragg Grating. *IEEE J Quantum Electron.* 2021;57:1–8.
35. Xing J, Li Z, Yu Y, Yu J. Design of polarization-independent adiabatic splitters fabricated on silicon-on-insulator substrates. *Opt Express.* 2013;21:26729–34.
36. Yun H, Shi W, Wang Y, Chrostowski L, Jaeger NaF. 2x2 adiabatic 3-dB coupler on silicon-on-insulator rib waveguides. *Photonics North. The International Society for Optical Engineering*; 2013.

Figures

Figure 1

Design of the FSR-free ADF. **a** Schematic 3D view of the ADF based on three coupled waveguides with a central grating-assisted F-P cavity. **b** Top view of the filter consisting of Bragg grating mirrors, tapered grating, and point-defects cavity, indicated within the dashed white rectangle in **a**. **c** Cross-section of the coupling region of the filter, indicated by the dashed orange line in **a**. **d** Top-view SEM image of the filter.

Figure 2

Optical simulations of the filter. **a** Calculated transmission spectra of the filter in the wavelength range of 1400–1630 nm at drop ports (D1 and D2) and through port (T1). **b** Simulated electric field distribution at 1400, 1516, and 1620 nm wavelengths.

Figure 3

FSR-free condition analysis. Contour maps of **a** the stopband of Bragg grating $\Delta\lambda_{sb}$, **b** the FSR_{FP} of F-P cavity, and **c** the ratio R ($R=\Delta\lambda_{sb}/\text{FSR}_{FP}$) as functions of Λ and d . Waveguide width d and L_c are 0.5 μm and 0 μm . **d** Simulations of the ratio R as a function of L_c and d . Waveguide width d and Λ are 0.5 μm and 316 nm. The dashed white and blue contour lines in **c** and **d** represent the value of $R=1$ and $R=2$, respectively. The pitch number of the Bragg grating and the tapered grating are 150 and 5.

Figure 4

Thermo-optic co-simulations of the filter. **a** Temperature distribution at different bias voltages based on a 3D simulation, sharing the same temperature color bar. **b** The optical response at D1 port by 3D FDTD simulation.

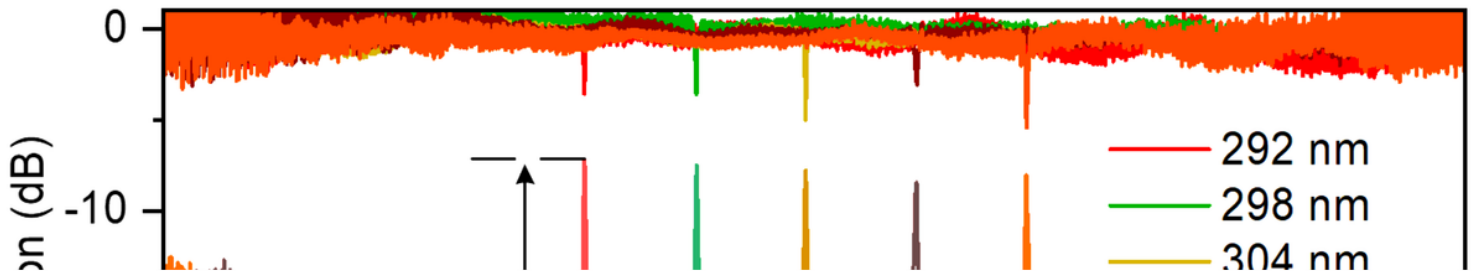


Figure 5

Measured transmission spectra of the fabricated devices with various pitches.

Figure 6

Dynamic tuning characterization. **a** Measured transmission spectra of the fabricated devices with various bias voltages, inset: zoom-in view of the peaks. **b** Resonant wavelength shifts with various heating powers. **c** 3-dB bandwidth and insertion loss variation with different heating powers.

Figure 7

Simulations of the design with the improved drop efficiency. **a** Simulated phase difference of the drop ports of the proposed ADF. The yellow star shows the resonance wavelength position. **b** Simulated transmission spectra of the improved device combining the 2×2 adiabatic splitter and the proposed ADF at the output port (Drop port). The insert shows the schematic of the improved device design.